AGU PUBLICATIONS

JGR

Journal of Geophysical Research: Space Physics

RESEARCH ARTICLE
10.1002/2013JA019495

Key Points:
- Case study of how many ion upflows can transport plasma to acceleration regions
- Ion flux in terms of plasma temperature
- Upflowing plasma acceleration and travel time

Correspondence to:
Å. Skjæveland,
asmund.skjaveland@fys.uio.no

Citation:
Skjæveland, Å., J. Moen, and H. C. Carlson (2014), Which cusp upflow events can possibly turn into outflows?, *J. Geophys. Res. Space Physics*, *119*, 6876–6890, doi:10.1002/2013JA019495.

Received 29 SEP 2013
Accepted 4 AUG 2014
Accepted article online 11 AUG 2014
Published online 25 AUG 2014

Which cusp upflow events can possibly turn into outflows?

Å. Skjæveland[1,2], J. Moen[1,2], and H. C. Carlson[3]

[1]Department of Physics, University of Oslo, Oslo, Norway, [2]Department of Arctic Geophysics, University Centre in Svalbard, Longyearbyen, Norway, [3]Space Weather Center, CASS, Utah State University, Logan, Utah, USA

Abstract Two sequences, before and after magnetic noon, respectively, of poleward moving auroral forms with associated upflows situated above the European Incoherent Scatter Svalbard Radar allowed close study of ion upflow dynamics. We find that flux intensity is correlated with plasma temperature and that upflowing plasma undergoes acceleration proportional to the slope of the velocity profile and to the velocity at each altitude. The potential for upflows to lift thermal plasma to regions where broadband extremely low frequency electric field activity can cause nonthermal acceleration leading to outflow is examined. Equations for estimating the travel time of upflowing plasma are presented. We find that around 40% of the observed upflow profiles with a unit number flux greater than $1 \times 10^{13}\,m^{-2}\,s^{-1}$ can transport plasma from 500 to 800 km altitude in less than 10 min, approximately the typical lifetime of pulsed upflow events. Almost all such profiles can transport plasma from 600 to 800 km in the same time span. Typical transport times for other altitude ranges are also presented. Post magnetic noon the background electron density was somewhat higher than prenoon due to transport of EUV-enhanced plasma, and the postnoon ion flux was somewhat weaker than prenoon.

1. Introduction

The motivation for this paper is to examine which ion upflows can lead to ion escape. We will examine the upflows in terms of ion number fluxes and examine whether and to what extent bulk ion upflows seen by incoherent scatter radar can transport plasma to altitudes where nonthermal acceleration mechanisms can create outflows. We will examine which measured parameters are the most important predictors of ion fluxes.

1.1. Ion Upflow and Outflow

It is known [e.g., *Shelley et al*., 1972, 1976; *Sharp et al*., 1981; *André and Yau*, 1997; *Yau and André*, 1997] that a large fraction of the magnetospheric heavy ions are drawn from the ionosphere, primarily from the ionospheric cusp and polar cap where the geomagnetic field lines extend deep into the magnetosphere [*Winglee*, 2000; *Winglee et al*., 2005, and references therein]. The bulk of O^+ escape from the ionosphere occurs in the ionospheric cusp, a phenomenon described as an "ion fountain" by *Lockwood et al*. [1985] and in the polar cap through the "polar wind" [*Barakat and Schunk*, 1983; *Yau et al*., 2007; *Ogawa et al*., 2009b].

In addition to purely scientific interest, ion upflow and outflow are of importance because narrow plasma upflows introduce transient mesoscale plasma density gradients [*Ogawa et al*., 2000; *Moen et al*., 2012] and meter-scale plasma density perturbations, both of which affect radio propagation through the ionosphere. The cusp also frequently contains strong thermospheric density enhancements, which will affect the orbit parameters of low polar orbiting satellites through atmospheric drag [*Lühr et al*., 2004].

Ion escape is a complex process, with no single mechanism thought to transport an ion from the *F* region to the magnetosphere. In general, it is useful to separate the problem into successive steps. The first step is the initial acceleration of bulk ion upflow events driven by ion heating and ambipolar diffusion as observed by incoherent scatter radars (ISRs) [*Wahlund et al*., 1992; *Ogawa et al*., 2000, 2003, 2010; *Buchert et al*., 2004; *Skjæveland et al*., 2011], sounding rockets [*Arnoldy et al*., 1996; *Lynch et al*., 1999; *Frederick-Frost et al*., 2007], and satellites in polar low Earth orbit in the *F* region ionosphere [*Coley et al*., 2003; *Ogawa et al*., 2003; *Lühr et al*., 2004; *Chaston et al*., 2006; *Lorentzen et al*., 2007; *Sadler et al*., 2012]. The second step is that upflow events that have reached sufficiently high altitudes are exposed to wave energies available in the topside

ionosphere/magnetosphere which drive nonthermal transverse acceleration of oxygen [*André and Yau*, 1997; *Strangeway et al*., 2005; *Chaston et al*., 2006; *Jacobsen and Moen*, 2010].

Magnetic reconnection at the magnetopause is the major energy transfer mechanism to the polar upper atmosphere in the daytime auroral zone, commonly referred to as the cusp/cleft ionosphere [*Cowley*, 1998, 2000; *Moen et al*., 1998, 2004a]. There are two major forms of energy transfer: soft electron precipitation giving rise to heating of the electron plasma observed as elevated electron temperature (T_e), and momentum/energy transfer observed as mesoscale ion flow channels associated with elevated ion temperature (T_i).

Ballistic motion alone cannot transform upflow to outflow. A plasma volume moving upward at 1000 m/s would, in the absence of external energization, travel at most 50 to 100 km before falling down again.

Wave activity is often but not always seen collocated with upflows and/or electron density depletions [*Lynch et al*., 1996]. Wave heating of ions in the topside ionosphere can accelerate thermal upflows into suprathermal outflows (conics and beams) [e.g., *Lynch et al*., 1996]. A number of different wave types can occur in the upper ionosphere upward, out to distances of several R_E [*André and Yau*, 1997; *Burchill et al*., 2004]. Broadband extremely low frequency (BBELF) fields are observed from the upper ionosphere to several R_E out. BBELF refers to electromagnetic fluctuations from 3 to 5 kHz down to quasi-static levels [*Lynch et al*., 1996; *Ivchenko and Marklund*, 2001; *Lorentzen et al*., 2007; *Jacobsen and Moen*, 2010].

Lund et al. [2000] mapped the occurrence rates of BBELF waves down to 1000 km altitude. Wave ion heating has been observed at lower altitudes, down to 520 km where data are primarily collected by sounding rockets [*Bonnell et al*., 1996; *Kintner et al*., 1996, 2000; *Burchill et al*., 2004, 2010; *Frederick-Frost et al*., 2007; *Lorentzen et al*., 2007; *Lynch et al*., 2007].

BBELF activity is primarily confined to the auroral oval, near the open-closed field-line boundary, and with an occurrence peak centered on the dayside cusp and a smaller peak on the nightside [*Lund et al*., 2000; *Ivchenko and Marklund*, 2001]. This morphology closely follows that associated with upward acceleration regions.

BBELF activity parallel to the geomagnetic field may manifest itself as Natural Enhanced Ion Acoustic Lines in incoherent radar spectra, which may lead to overestimated electron densities and spurious temperatures [*Lorentzen et al*., 2007].

Statistical work by *Buchert et al*. [2004] and *Ogawa et al*. [2009a] showed that ion upflows above the European Incoherent Scatter Svalbard Radar (ESR) occurred for any magnetic local time (MLT) and *Kp*, but were most common around magnetic noon, with the peak at 13 MLT (upflow occurrence rate 18%) and somewhat more upflows prenoon (8–10%) than postnoon (5–10%, with a clear minimum around 18–20 MLT). For large *Kp*, downflows were commonly observed on the dayside, with downflow occurrence rate exceeding upflow occurrence in the interval 12–15 MLT. This increase in downflow throughout the dayside was interpreted as ballistic return of upflows occurring equatorward of the ESR when the auroral oval was expanded. The average ion flux in upflow events was not found to vary much with *Kp*.

Reconnection energy deposition heats both the ions (T_i) (response time ~1/2 min) and the upper thermosphere (T_n). The T_n response time is strongly dependent on altitude and ion velocity (v_i) [*Carlson et al*., 2012] but is as short as several minutes near or above ~200 km. Particle precipitation near the onset of these events also heats the electron gas (T_e), and in the dark cusp can raise the frictional drag heating to altitudes near or above ~200 km [*Carlson et al*., 2012].

This raising of the frictional heating altitude has consequences for the thermosphere. The thermospheric density was observed by the CHAMP spacecraft to be enhanced in the cusp at 400 km altitude, sometimes up to double the background level [*Lühr et al*., 2004; *Watermann et al*., 2005]. This can be explained as upwelling of the upper thermosphere driven by ion frictional drag heating near and above ~180 km. *Carlson et al*. [2012] solved the longstanding problem of reproducing the density doubling. Using a 3-D time-dependent modeling including the "fountain" effect (the heated and upwelling neutral gas, not confined by the magnetic field, spreads sideways from the heating region and downflows in the nonheated thermosphere), they found that ~5 min of heating was sufficient to reproduce the observed enhancements, corresponding to the duration of transient ion heating events in the cusp ionosphere.

Heating by soft electron particle precipitation alone cannot produce the observed enhancement in time order of minutes [*Sadler et al*., 2012]. *Carlson et al*. [2012] clarify that while realistic soft particle fluxes do not deposit enough energy to produce significant upwelling, in local darkness they define the electron density profile, which in turn directs the frictional drag heating to high enough altitudes that frictional drag heating produces thermospheric upwelling.

Enhanced electron temperature is tied to electron precipitation, while enhanced ion temperature is tied to ion-neutral frictional heating due to enhanced ion flow channels. T_e enhancements will accompany T_i enhancements at the onset of magnetic reconnection events, as electrons precipitate out of the newly opened flux tubes. The magnetic curvature force drives high-speed horizontal plasma flow jets in the ionosphere after reconnection [*Valladares et al*., 1998]. Current sheets of upgoing or precipitating electrons bound the edges of this driven flow channel [*Southwood*, 1987; *Moen et al*., 2012]. That CHAMP sees density/drag enhancements collocated with fine current sheets was one of the pieces of supporting evidence cited by *Carlson et al*. [2012] for their explanation of the density doublings as due to energy deposition associated with magnetic reconnection events (which also have accompanying fine current sheets). More generally, the coupling among current sheets, electric fields, and plasma flow channels has been discussed by *Moen et al*. [2004b].

Moen et al. [2004a] revealed the pulsed nature of ion upflows simultaneous to and collocated with poleward moving auroral forms (PMAFs). The aurora near magnetic noon frequently exhibits PMAFs [*Sandholt et al*., 2002]. These forms are linked to magnetopause reconnection [*Sandholt et al*., 1990] and are collocated with transient ion upflow events [*Moen et al*., 2004a]. PMAFs have a typical duration of ~5–10 min [*Sandholt et al*., 1989, 1990], and the collocated ion upflow events are believed to be of similar duration. This is consistent with a pulsed-reconnection cusp model [*Lockwood et al*., 1993], in which PMAFs are tied to distinct reconnected flux tubes with similar but independent history and evolution. Flow channels created by pulsed reconnection have a typical duration of 10–20 min [*Lockwood et al*., 1990; *Rinne et al*., 2011].

The main objective of this paper is to examine which upflow events are more likely to reach the region where available wave energy or upward acceleration processes can lead to ion escape. We also present estimates of the time it takes an upflow event to move plasma from various altitudes up to 1000 km altitude, and whether this is possible, within the typical duration of a pulsed dayside upflow event.

The paper is organized as follows:

First, we will describe the principles behind the assumption of flux conservation, which is used in the data analysis. Then we will give a brief description of the instrumentation. In the observation section we will present the raw observations and the results from the data analysis. The results will be examined and put in the context of earlier work in the discussion section. Finally, the main results will be summarized, and conclusions will be presented.

1.2. Nomenclature

In this paper we use the terms "ion upflow" to describe thermal bulk ion flow upward along magnetic field lines, and "ion outflow" for plasma that has escaped or is in the process of escaping from the Earth's gravity. Ion velocities are denoted by v_i for velocities in general. In the appendix we introduce the terms $w(t)$ and $v(z)$ for, respectively, the time-dependent velocity and the altitude-dependent velocity of an upflowing parcel of plasma in the field-aligned direction.

The radar data consist of a sequence of field-aligned measurements. Individual radar measurements are referred to as "profiles" when referring to a range of altitudes of data.

We use the term "ion flux" as shorthand for "ion number flux density." We calculate the flux by multiplying measured electron density (n_e) by the field-aligned bulk ion velocity (v_i). The ion number flux density per unit area will decrease with altitude because the magnetic flux tubes grow wider with altitude, and the ion flux in a flux tube is spread across a larger cross section at higher altitudes. All ion fluxes presented here have been scaled to the geomagnetic field strength at 500 km altitude to remove this effect from the figures. All fluxes discussed are upward unless otherwise specified.

Prenoon and postnoon refer to before and after magnetic noon (approximately 0850 UT).

1.3. Flux Conservation

Starting with the continuity equation, assuming hydrostatic equilibrium and ignoring horizontal transport, we have

$$\frac{\partial n}{\partial t} + \frac{1}{A}\frac{\partial (\mathrm{Anv})}{\partial z} = P - \mathrm{Ln} \tag{1}$$

(From equation (12.18) in *Schunk and Nagy* [2009, p. 458])

Where n is the electron density, v the vertical plasma drift (along z), P the ionization production rate, and L the chemical loss frequency. The quantity $(1/A)\ \partial A/\partial z$ accounts for the divergence of the geomagnetic field with altitude. In the ionosphere this term can be removed by normalizing the unit flux to the geomagnetic field at a reference altitude.

In a steady state the electron density does not change, and for the topside ionosphere, we have negligible production and recombination: $P \approx 0; \mathrm{Ln} \approx 0$

$$\frac{\partial n}{\partial t} = -\frac{1}{A}\frac{\partial (\mathrm{Anv})}{\partial z} \tag{2}$$

$$\frac{\partial n}{\partial t} \sim 0 \Rightarrow -\frac{\partial (\mathrm{nv})}{\partial z} = 0 \Leftrightarrow \mathrm{nv} = \mathrm{const.} \tag{3}$$

We therefore find that when production and recombination rates are sufficiently low, we expect, to a first approximation, to find the number flux of plasma to be constant with altitude. This continues with increasing altitude until another term needs to be added to the equation. For O^+ at some further altitude (order of 1000–5000 km) instability processes enter, and acceleration terms can lead to escape velocity. When a plasma reaches supersonic speeds, the $v(\mathrm{d}v/\mathrm{d}r)$ term in the momentum equation starts to dominate. Therefore, as v (and Mach number) increases, $\mathrm{d}v/\mathrm{d}r$ decreases; and then for high Mach numbers v tends to go constant. This is true in the polar wind [*Schunk*, 1988] but not before the O^+ has passed through an acceleration region which can make escape possible.

2. Instrumentation

The data presented are incoherent scatter radar data from the European Incoherent Scatter (EISCAT) Svalbard Radar (ESR), located outside Longyearbyen, Svalbard, at 78.15°N, 16.03°E, and optical data from the Meridional Scanning Photometer (MSP) in Ny-Ålesund, Svalbard, at 78.92°N, 11.92°E. The MSP is located approximately 123 km NW of ESR and had clear skies for the duration of the observation. The Auroral Station in Longyearbyen was not used due to haze and clouds.

In addition, ion velocity and density data from the Special Sensors-Ions, Electrons, and Scintillation (SSIES) instrument during a nearby pass of DMSP F13 were used to verify high-altitude ESR velocities and fluxes.

3. Observations

Simultaneous optical and incoherent scatter radar observations were carried out on Svalbard on 20 December 1998. The *Kp* index was 3− (2.7), and the $F_{10.7}$ index was 130.4. Figure 1 shows data from ESR (Figures 1a–1c) and the MSP (Figure 1d). The ESR was running the GUP3 mode, pointing parallel to the geomagnetic field (azimuth 180.6°, elevation 81.6°). We downloaded processed data from the Madrigal database. The data were processed with 60 s integration time. The white line at 32° south in Figure 1d marks the MSP elevation angle closest to the ESR beam at 250 km altitude. The yellow line in Figure 1d shows the north-south movement of the DMSP F13 geomagnetic foot point (in Altitude Adjusted Corrected Geomagnetic Coordinates) as it passed close by the radar beam.

The ESR was running in this mode from 0600 until 1200 UT. The MSP was running until 1100 UT. The data shown are for 0600–1100 UT, centered on the cusp aurora. Magnetic noon was around 0850 UT.

The MSP data shows that the auroral oval expanded and contracted during the observation period, so that the radar beam was equatorward of the auroral oval 0600–0615 UT and 0745–0900 UT, inside the aurora 0615–0745 UT and 0900–0940 UT and poleward of the auroral oval or near its poleward boundary 0940–1100 UT. In addition, sequences of poleward moving auroral forms (PMAFs) were seen 0600–0940 UT.

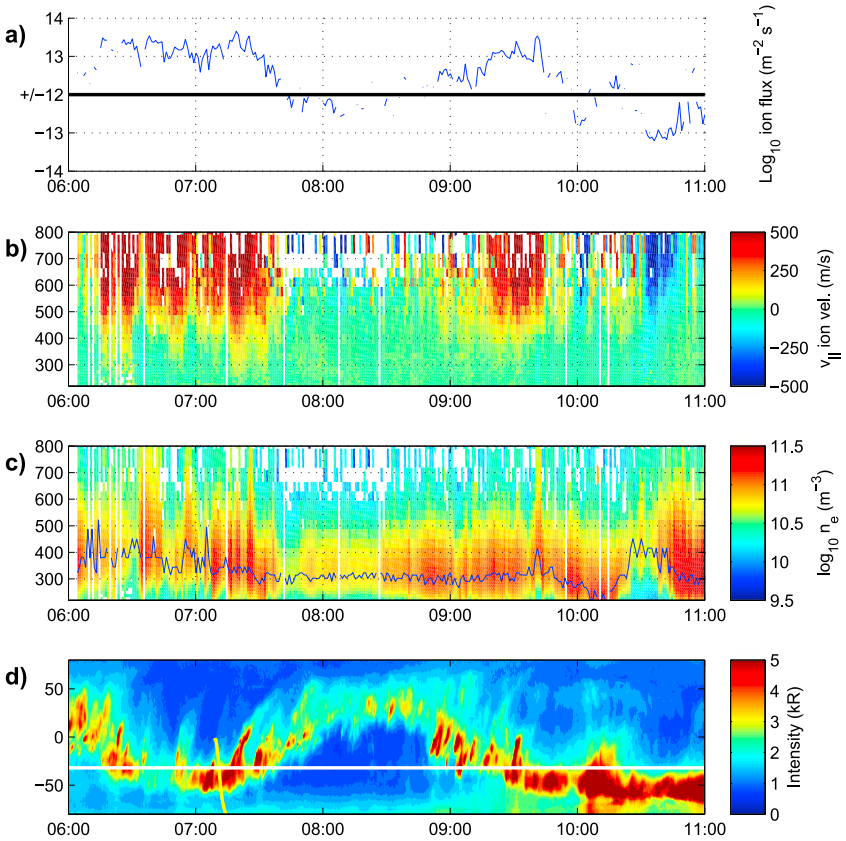

Figure 1. (a) Upward and downward logarithmic ion flux. (b) Field-aligned ion velocity. (c) Logarithmic electron density. The blue line marks the altitude of the F_2 density maximum. (d) MSP data of 630.0 nm, with north to south motion of DMSP F13 marked with yellow line. The white line marks the location of the ESR radar beam mapped to 250 km altitude.

Figure 1a shows upward and downward $\log_{10}$ ion flux, where positive values are upward flux and negative values are downward flux. One flux value is assigned to each radar profile, by a method to be explained in section 4. Only values exceeding $\pm 1 \times 10^{12}\,m^{-2}\,s^{-1}$ are shown in this plot, as measurements of fluxes weaker than this limit have large relative error bars. Most profiles with flux around or exceeding $1 \times 10^{13}\,m^{-2}\,s^{-1}$ have a common general shape: a "source region" at low altitudes where flux increases rapidly with altitude and a region of low variation of flux with increasing altitude above this source region. Examples can be seen in Figure 4a. We call profiles with this property "constant-flux" profiles.

The source region is generally located between the F_2 maximum density and some 100–200 km above. For most profiles, this locates the transition from source region to constant-flux region at 400–500 km altitude.

Ogawa et al. [2009a] found that typical ion fluxes for the 9–15 MLT sector during upflows, for these *Kp* conditions, were in the range $7 \times 10^{12}\,m^{-2}\,s^{-1}$ to $3 \times 10^{13}\,m^{-2}\,s^{-1}$, mostly above $1 \times 10^{13}\,m^{-2}\,s^{-1}$. We also found that for this data set upflow fluxes below $1 \times 10^{13}\,m^{-2}\,s^{-1}$ frequently did not reach a well-defined constant-flux level but instead continued to have significant scatter throughout the radar profile. Although there is no sharp limit for when the flux will be constant or not, we have selected $1 \times 10^{13}\,m^{-2}\,s^{-1}$ as a threshold for where the flux was more or less likely to be constant with altitude. We will refer to fluxes exceeding $\pm 1 \times 10^{13}\,m^{-2}\,s^{-1}$ as "strong flux" for short, and fluxes in the range $\pm 1 \times 10^{12}$–$1 \times 10^{13}\,m^{-2}\,s^{-1}$ as "weak flux."

The F_2 peak electron density altitude was around 300–400 km between 0600 and 0730 UT (0310–0740 MLT), 300 km between 0800 and 1000 UT (1110–1310 MLT), and 200–300 km between 1000 and 1200 UT (1310–1510 MLT). The peak electron density was generally highest in the prenoon sector between 0600 and 0730 UT and after 1000 UT. Ion and/or electron temperatures were always elevated during upflows.

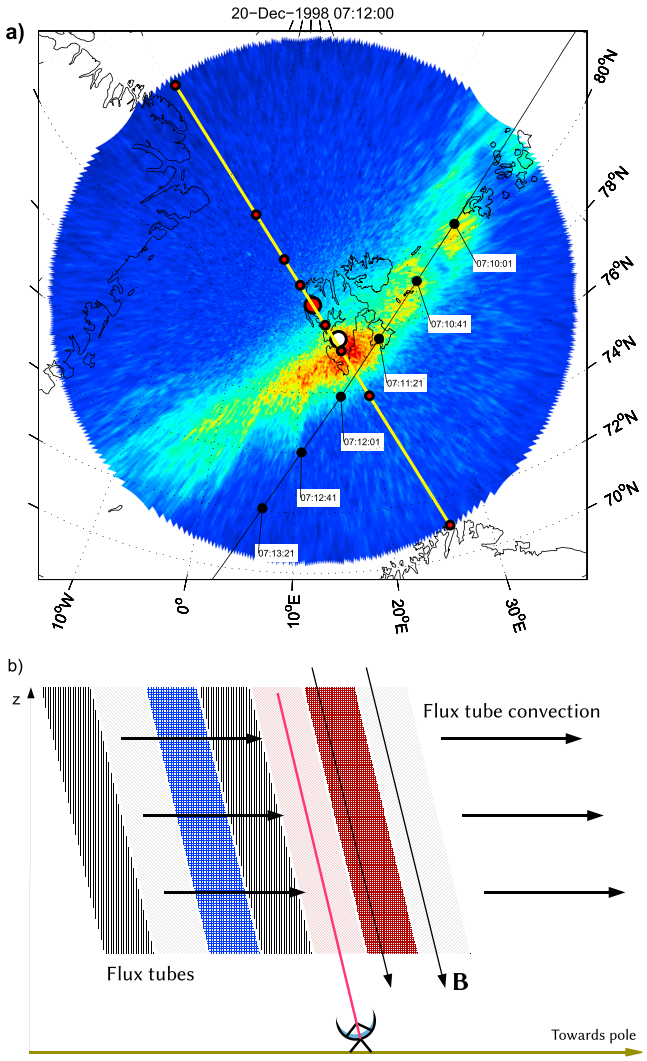

Figure 2. (a) Aurora (630.0 nm) projected onto map of Svalbard and surrounding regions, assuming 250 km emission altitude. Color scale in arbitrary units. The large red dot indicates MSP location; the yellow line indicates MSP scan plane. Red dots along line mark 20, 40, 60, and 80° zenith angle north/south. The white dot indicates location of ESR radar beam at 250 km altitude. The black line shows the path of the DMSP F13 geomagnetic foot point, mapped to 250 km altitude. Geographical coordinates are shown. (b) Illustration of poleward component of convection of flux tubes across the radar beam. The flux tubes are convecting poleward, toward the right in this figure. For typical large IMF B_y, the largest component of flow shortly after reconnection is out of the page, in the east-west direction as determined by the magnetic tension direction. After relaxation of the magnetic tension (10–20 min), the transient mesoscale flow channel relaxes into background transpolar flow.

The DMSP F13 spacecraft passed close by Svalbard and crossed the auroral oval at approximately 0711 UT. The geometry of the overflight is shown in Figure 2a, along with the MSP scan plane and ESR beam location at 250 km altitude. The DMSP F13 track is mapped geomagnetically to 250 km altitude. Figure 2b shows the conceptual picture of a train of separate flux tubes convecting poleward across the radar field of view. Figure 3 shows ion flux data from ESR and DMSP (Figure 2a) and MSP data (Figure 2b), with the north-south motion of DMSP F13 shown as a yellow line in the MSP data. The white line again shows the location of the radar beam in the MSP field of view at 250 km altitude.

Vertical ion velocity and electron density data from the SSIES instrument confine the upward ion flow mostly to the optically active auroral oval. The ion flux data show a sharp boundary near the equatorward oval edge, with considerable flux poleward of the boundary and very little equatorward of it. This is consistent with ESR data (Figures 1a and 1b), which sees strong upflow and flux in the auroral oval when PMAFs are present

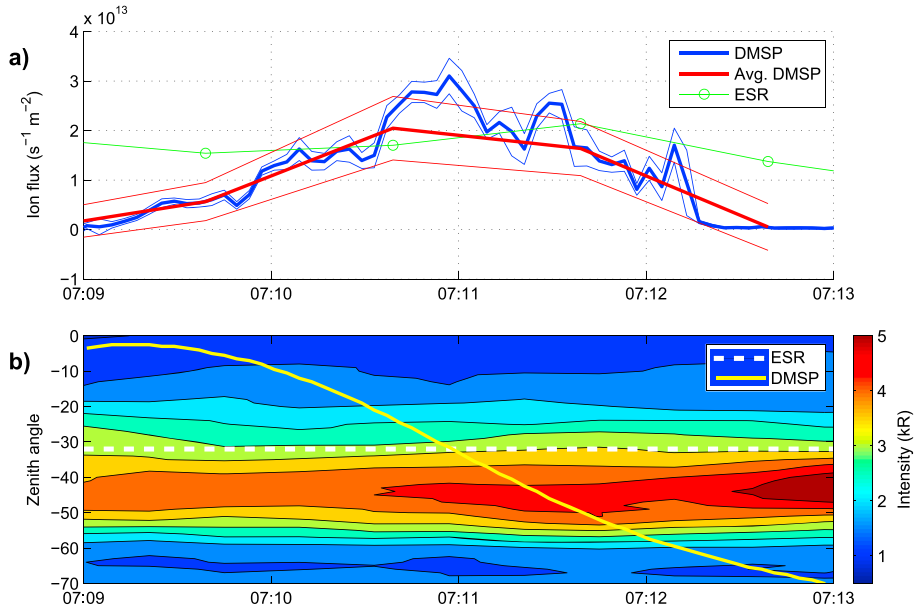

Figure 3. (a) Vertical ion flux measured by DMSP F13, 4 s data and 1 min averages, and field-aligned flux measured by ESR. Thin lines around DMSP data indicate 1σ error bars. (b) MSP data of 630.0 nm. The white dashed line indicates location of the ESR radar beam, and the yellow curve indicates geomagnetic north to south motion of the DMSP F13 foot point.

(0614–0745 and 0855–0940 UT) and no upflow equatorward of the oval (0600–0615 and 0830–0855 UT) and primarily downflow poleward of the oval (1015–1100 UT).

The proximity of DMSP F13 to the ESR beam during the 0711 UT pass allowed us to verify that the field-aligned ion velocities and fluxes ESR found were consistent with vertical ion velocities and fluxes measured in situ by DMSP F13. Only two ESR data points (0710–0711 and 0711–0712 UT) are close enough to DMSP in space and time for direct comparison. The velocities measured by DMSP were, respectively, 35 m/s and 150 m/s higher than those extrapolated from ESR data, and DMSP ion fluxes were, respectively, 120% and 70% of ion flux measured by ESR. The spacecraft data additionally show that the cusp has velocity, and flux structure significantly finer than the ESR can resolve with an integration time of 60 s. Figure 3a shows both 4 s measurements and 1 min averages of DMSP data.

3.1. Plasma Convection and PMAFs

The radar is observing in the field-aligned direction while plasma is convecting across the beam at speeds of 300–1000 m/s (*Skjæveland et al.* [2011] based on Super Dual Auroral Radar Network measurements), though importantly during magnetic reconnection events, flow jets can reach 2000–3000 m/s. Therefore, the radar sees new plasma for each measurement. This is illustrated conceptually in Figure 2b, which shows the poleward component of motion of the train of flux tubes. The upflow we describe in this paper occurs over plasma flow jets. As summarized in [*Carlson*, 2012], we can say several things about flow jet morphology. Within plasma flow jets the plasma convects in the interplanetary magnetic field (IMF) B_y magnetic tension direction for ~15 min, with a transient optical brightening during the initial ~5 min coincident with a transient enhancement of electron density below 200 km, and a continuing optical signature on the *E* field convergence side of the pair of flow channel north-south boundaries (the boundary with an incoming electron sheet, i.e., current carriers of the outgoing current sheet boundary). For IMF B_y much greater than zero, the flow jet is initially largely east/west (direction controlled by the sign of IMF B_y). It also has a poleward component of motion, which when tracked by MSPs readily shows an associated optical signature, referred to as a PMAF. There is no reason to believe that adjacent magnetic flux tubes along this poleward flow direction, during this 5 min, should behave with any significant difference from each other. We expect them to be similar to each other in precipitating electron flux until they have been depleted of previously trapped particles, and in flow shear until the magnetic curvature force relaxes and the flow jet relaxes back into the slower background transpolar plasma convection flow field. There is no external force that should change the

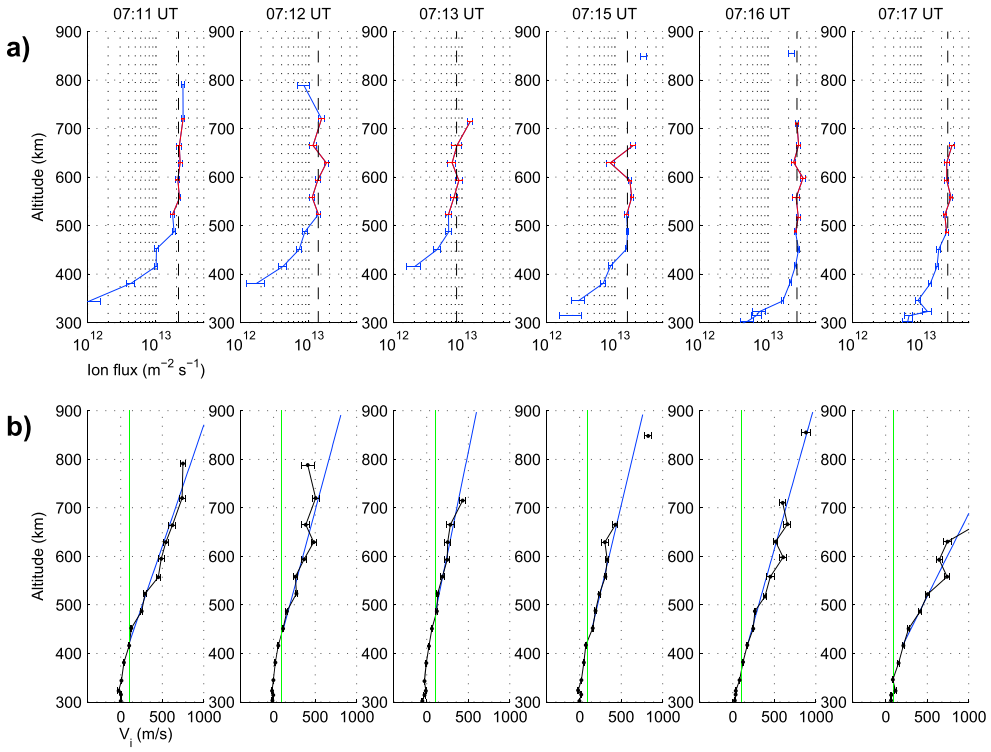

Figure 4. (a) Ion flux profiles. Red data points are those used in averaging. Vertical black line shows averaged flux. The drop-off of flux with altitude due to the divergence of the geomagnetic field has been removed from the figure. (b) Observed ion velocities with linear fit. Vertical green line shows 100 m/s threshold.

behavior of the plasma in the flux tube other than its own heating, thermal time constant, and gravity once the heat source has expired. *Rinne et al.* [2010] showed by direct observation how pulsed reconnection events lead to a train of flow channels, each new event pushing the older flow channels further into the polar cap. Typical north-south extent of flow channels tied to newly reconnected flux tubes is ~100–300 km, with east-west extent exceeding 1000 km [*Lockwood et al.*, 1990; *Rinne et al.*, 2011].

4. Data Analysis and Discussion

The ion fluxes measured by the SSIES instrument on board DMSP F13 in the 0711 UT pass are comparable to those measured by ESR, which gives us the confidence to assume that the ESR flux data are reasonably accurate.

Figure 4a shows ion fluxes for selected profiles 0711–0717 UT except 0714. Each profile was assigned a flux value by averaging the range gates between 100 km above the F_2 peak (typically 400–500 km altitude) and 700 km altitude. The data points used in the averaging are shown in red in the profiles, and the vertical dashed line shows the average value. Data gaps occur for a number of reasons, such as radar echoes from passing satellites or debris, or poor spectral fits due to low signal-to-noise ratio. We have filtered out data points flagged for poor quality and those with too large error bars. For 0714 the entire radar profile was invalid, perhaps due to transient external noise.

Figure 4b shows the ion velocity for the same profiles. These profiles are part of an upflow event tied to a PMAF. The vertical green line indicates a 100 m/s threshold following the upflow definition of *Ogawa et al.* [2009a]: At least three simultaneous data points, consecutive in altitude, with velocity exceeding 100 m/s, and where each point has velocity higher than the preceding one. The blue line is a linear regression of all data points which exceeded the velocity threshold and which were above the last data point to not exceed the threshold.

The flux profiles shown in Figure 4a serve as examples of the approximately constant nature of the ion flux in strong flux upflow events. When the flux was much below 1×10^{13} m^{-2} s^{-1}, the flux profiles generally had large scatter.

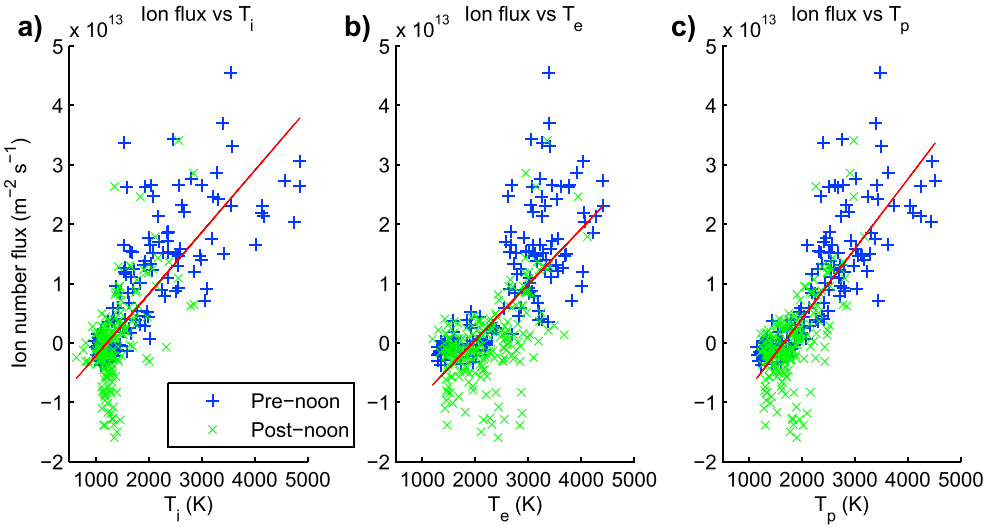

Figure 5. Average (a) ion, (b) electron, and (c) plasma temperature between 300 and 500 km altitude, plotted versus ion flux.

4.1. Correlation of Flux With Temperatures and Other Parameters

We explored the correlation of the ion flux with the other measured parameters.

There was very low correlation between flux and topside electron density, and essentially no correlation between flux intensity and peak electron density. Conversely, there was a strong correlation with ion velocity, suggesting that the observed variation in electron density is not large enough to significantly influence flux intensity. This is also the case for the DMSP vertical flux data.

Plasma heating is a strong driver of ion upflows [*Wahlund et al.*, 1992; *Burchill et al.*, 2010; *Skjæveland et al.*, 2011]. The observed ion flux is tied to plasma temperatures. For temperatures we found the strongest relationship to be between ion flux and the averaged plasma temperature ($T_p = (T_i + T_e)/2$). Figure 5 shows a scatterplot of these relationships for (Figure 5a) T_i, (Figure 5b) T_e, and (Figure 5c) T_p. The blue plus signs represent premagnetic noon data and the green crosses postnoon data. The straight line is an unweighted linear fit of all the data, without distinguishing prenoon and postnoon. One marker represents one radar profile. For T_i we find a coefficient of determination $r^2 = 0.56$. For T_e the corresponding number is $r^2 = 0.50$, and for T_p $r^2 = 0.63$. The figure shows all 337 profiles obtained during the time interval from 0600 to 1200 UT, but the pattern is present also when the data set is divided into smaller regions based on the location of the auroral oval relative to the radar beam. The temperatures were averaged over 400–500 km altitude. Although there is significant scatter and clumping, a trend is clear: we find that cold plasma is dominated by weak or downward flux, and for $T_p > 2000$ K nearly all profiles show upward flux, with flux intensity increasing with temperature.

The observed correlations may be reasonably typical for this type of day (midwinter, dark ionosphere, moderate *Kp*, and negative IMF B_z) but are probably not representative for the cusp ionosphere as a whole and should not be taken as such. When the polar ionosphere is sunlit densities can reach much higher levels [e.g., *Moen et al.*, 2008]. For a dramatic counterexample of change in observed ion flux driven by variation in electron density on the nightside, see *Semeter et al.* [2003]. Instead, we observe that this is a data set in which the variation in ion flux is primarily driven by plasma heating rather than ionization or patch convection.

We will now try to quantify how many upflow profiles will be able to transport plasma from the *F* region to the topside ionosphere, where suprathermal acceleration mechanisms become increasingly important.

4.2. Upflow Travel Time

In this paper we only have data on thermal upflows. The possible effect of nonthermal acceleration mechanisms expected for, e.g., ion conics, beams and transversely accelerated ions is not resolved by standard ISR analysis, which assumes a thermal Maxwellian plasma distribution.

Table 1. Travel Times and Percentages of Events With Travel Times Less Than 10 min for Observed Strong Flux Profiles[a]

From Altitude (km)	Travel Time to 600 km (min)	Percentage Less Than 10 min	Travel Time to 800 km (min)	Percentage Less Than 10 min	Travel Time to 1000 km (min)	Percentage Less Than 10 min
400	10–25 [12–25, 16#]	6 [0]	15–30 [19–33, 8#]	0 [0]	17–35 [n/a, 0#]	0 [n/a]
450	5–15 [6–15, 43#]	57 [60]	10–25 [12–20, 28#]	8 [0]	12–25 [15–22, 21#]	0 [0]
500	3–8 (2–7) [3–8, 53#]	95 (97) [98]	6–15 (6–16) [8–17, 38#]	42 (44) [23]	9–23 (7–21) [12–19, 29#]	11 (16) [0]
550	2–4 (1–3) [1–4, 64#]	100 (100) [100]	4–12 (4–12) [5–13, 49#]	76 (79) [77]	7–17 (6–18) [9–17, 37#]	34 (39) [13]
600			3–10 (3–9) [4–9, 53#]	97 (96) [100]	5–14 (4–15) [6–14, 45#]	57 (63) [71]
700			1–4 (1–4) [2–4, 63#]	100 (100) [100]	3–10 (2–10) [4–9, 53#]	97 (93) [100]
800					2–6 (1–6) [2–5, 60#]	100 (99) [100]

[a]Numbers show travel time ranges and percentages for v_i fit, time-independent assumption (flux fit, time-independent assumption) [v_i fit, time-dependent assumption]. Number marked # in brackets is the number of travel time data points for that altitude range for the time-dependent calculations. The time independent assumption moves with the flux tube and satisfies conservation of flux; the time dependent applies flux tube data only while overhead within the radar field of view. The time ranges exclude the longest 5% of travel times; see text. Flux fit is not calculated for 400 and 450 km starting altitudes.

Upflowing plasma that does not escape as outflow would be expected to return as downflow. Thermal downflow is frequently observed by ESR poleward of and/or after upflow [e.g., *Ogawa et al*., 2009a], but of lesser intensity than the upflow. This has been interpreted as ballistic return of previous upflow, possibly spread over a larger area, which cannot be easily sampled by pencil-beam radar such as ESR. It is therefore not trivial to compare upflow and downflow to measure how much plasma has been uplifted, if any.

It is necessary to smooth the radar data to calculate the travel time of an upflowing plasma volume. We observe that, in strong ion upflows, the ion velocity profiles increase approximately linearly with altitude above the F_2 density maximum (see Figure 4b). We can therefore smooth the velocity profiles by means of a linear regression (v_i fit). Alternatively, when we calculate a constant-flux value for each profile, we can fit an exponential to the n_e profile and from this reconstruct a smoothed velocity profile (flux fit).

Since the radar was looking directly up the geomagnetic field with the plasma convecting across the field of view, it is not possible from the radar data alone to separate temporal variation occurring in the plasma from spatial structures convecting across the radar beam. We therefore made independent calculations of travel time based on two mutually exclusive assumptions. In the first case, we assume that the velocity profiles inside the convecting flux tubes are static for the duration of the upflow events (time-independent $v_i(z)$), in other words that from the reference frame of an upflowing volume of plasma within a moving flux tube, the velocity profile $v_i(z)$ does not change with time. In the second case, we assume that the variation in time seen by the radar is equal to the time variation of $v_i(z)$ inside each flux tube as it convects overhead (time-dependent $v_i(z)$).

We combined the two smoothing methods with the two mutually exclusive assumptions about time independence/dependence into three methods of estimating travel time.

Method 1: v_i smoothing, time-independent $v_i(z)$
Method 2: flux smoothing, time-independent $v_i(z)$
Method 3: v_i smoothing, time-dependent $v_i(z)$

The resulting travel times are shown in Table 1. We do not show the combination flux smoothing and time-dependent $v_i(z)$ since the two smoothing methods give very similar results for travel times.

In the case of Method 1, the travel time from altitude z_0 to z_1 has an analytical solution of exponential form, shown in Appendix A. In the other cases we have used numerical integration. Methods 1 and 2 give one travel time value per radar profile, while Method 3 requires a continuous sequence of upflow measurements.

For Methods 1 and 2 we only considered strong flux profiles. For Method 3 we required that the initial profile in the integration was a strong flux profile. The integration was halted, and the travel time computation considered to have failed if the integration encountered a data gap wider than one radar profile (60 s) or if the upflow stopped before the target altitude was reached.

Note that good radar data are scarce above 800 km, so the travel time results up to 1000 km are partly based on extrapolation for all three methods. The data points that do exist seem to tend to follow the linear trend for v_i when the error bars are small, but as the statistics are poor the travel times we report for the highest altitudes should be treated with caution.

Because the calculation method occasionally produced very long tails on the distributions of travel times, the 5% longest travel times were excluded from the time ranges.

For each method we show the spread of travel times for that altitude range and the percentage of the profiles for which a travel time could be computed where the travel time was less than 10 min. Data for Method 1 are shown first, then Method 2 in parentheses (), then Method 3 in square brackets []. Method 2 is not shown for starting altitudes 400 and 450 km and below since the flux was generally not constant below 500 km altitude and so the smoothing algorithm based on constant flux is not valid.

Method 3 assumes that the time variation seen in v_i is representative of what happens inside the reconnected flux tubes. Since the flux tubes convect across the radar field of view in 2–5 min the method cannot be considered a direct measurement of vertical motion of longer duration than 5 min. When travel time exceeds 5 min, the method is mixing velocities from different flux tubes and it is in effect averaging the upflow seen by a longer period of observation.

The number of successful travel time calculations that make up each time-dependent statistic is shown along with the range of times, marked with a # sign. Method 3 requires a continuous period of upward ion velocity, and this requirement is the reason for the dropoff in number of data points with increasing altitude for all altitude ranges, as well as the poor statistics for computations starting at low altitudes. Ion velocities in the 400–450 km range are low and occasionally downward even for profiles with upflow at higher altitudes. Since most of the travel time is spent at lower and slower altitudes, Method 3 is likely to encounter low-altitude downward motion which will stop the computation even for profiles with overall upward flux.

The percentage of upflow times less than 10 min can vary among the three methods for the same altitude range when the travel time range includes the cutoff time of 10 min. This is because the travel time distributions are similar but not identical for the three methods, and so the cutoff time can end up on different sides of the distribution peak for the different methods. This effect is most apparent where Method 3 has very few samples.

The two time-independent methods only consider one velocity profile per data point and have 62 to 75 travel time computations for each travel time range.

For upflow to become outflow, plasma must be lifted high enough that wave energization is likely. PMAFs have a typical lifetime of 5–10 min [*Sandholt et al*., 1989, 1990; *Karlson et al*., 1996] and have been found to be linked to upflow events [*Moen et al*., 2004a]. The V-shaped upflow events were interpreted as signatures of quasi-static inverted-V potential structures [*Hoffman and Lin*, 1981; *Dombeck et al*., 2013] convecting across the radar beam [*Moen et al*., 2004a]. It is clear from Table 1 that plasma from 400 km cannot reach 800 or 1000 km in the average lifetime of one upflow event (10 min) and is unlikely to reach 600 km. However, plasma from 500 km may well reach 800 km altitude, and plasma transport from 600 to 800 km is very likely.

The radar beam pointed in the geomagnetic field-aligned direction, 8.4° off vertical toward the south. This small deviation from the vertical adds 3% to the travel time compared to vertical flight between the same altitudes.

If all events (both strong and weak flux profiles) are considered, 30% of the upflow profiles had travel time less than 10 min from 600 km to 1000 km altitude by Method 1 or 61% from 600 to 800 km. Of the weak flux profiles, only 9% had travel time less than 10 min from 600 to 1000 km or 32% from 600 to 800 km. No profiles, weak or strong, had travel times less than 10 min from 400 to 800 km. This implies that few upflow events are able to transport plasma from 400 to 800 km in one go.

As stated in the theory background, BBELFs are believed to occasionally occur down to below 600 km altitude. In this case plasma lifted from as far down as 450 km may have a fair chance of being accelerated by waves. The effectiveness of such an uplift is beyond the scope of this paper.

The Method 1 and Method 2 travel time calculation assumes a simple all-on/all-off upflows, with the velocity profile held constant for the duration of the upflow. A more realistic model might include a ramp-up and ramp-down of upflow intensity similar to PMAF intensity variation [*Sandholt et al*., 1989]. We have chosen to assume no time variation in the velocity profile for each travel time calculation because we do not have good knowledge of the time evolution of the velocity profile within the flux tube. While adjacent flux tubes are similar, as described in section 3.1, they are not identical and spatial variation in ion velocity profile must be allowed for in a sequence of upflowing flux tubes. The radar is looking parallel to the field lines and looking

up each flux tube as it passes overhead. The time variation observed in the velocity profile (see Figure 4b) is therefore due to the convection of new flux tubes into the field of view. The variation from minute to minute must be assumed to be at least partially spatial.

As explained in section 3.1, we expect adjacent flux tubes reconnected under the same IMF conditions to be similar, and as such the travel times we present by Method 3 are representative of the typical upflow, although it does not tie into distinct upflow events.

4.3. Effect of Intake of Solar EUV-Enhanced Plasma

To make it easier to follow the description below from Figure 1c, we will use both linear and logarithmic units for electron density in the following two paragraphs.

During PMAF and upflow activity, the electron density was variable. From 0600 to 0745 UT the electron density peak level was approximately $10^{11.4}$ (2.5×10^{11}) m^{-3}, and the background level was approximately $10^{10.5}$ (3.2×10^{10}) m^{-3}. During the quiet period, the electron density remained low, at $10^{10.5}$–$10^{10.7}$ (3.2–5.0×10^{10}) m^{-3} until 0830 UT.

Around 0830, while the auroral oval was contracted to poleward of the radar beam, solar EUV-enhanced plasma convected poleward into the radar field of view [*Pryse et al.*, 2004], establishing a new background electron density of $10^{10.9}$ (7.9×10^{10}) m^{-3}. Around 0900 UT (1210 MLT) the auroral oval again expanded equatorward across the radar beam. The background level remained around $10^{10.9}$ (7.9×10^{10}) m^{-3} and the new peak level was $10^{11.3}$ (2.0×10^{11}) m^{-3}. Upflow activity after magnetic noon (0850 UT) was somewhat less intense than prenoon, and plasma temperatures were slightly lower. Upflow activity ceased around 0950 UT (1300 MLT). This difference between premagnetic noon and postnoon is reflected in the different clustering in Figure 5 of prenoon data (blue plus signs) and postnoon data (green crosses).

5. Summary and Conclusions

The question we set out to explore was the following: can incoherent scatter radar data tell us if an upflow event will cause ion escape?

We have described characteristics of the ion flux during two consecutive extended series of upflows that occurred on 20 December 1998 over Svalbard as the auroral oval contracted and expanded over the ESR. We noted that profiles with flux exceeding $1\times10^{13}\,m^{-2}\,s^{-1}$ were likely to be of constant-flux type, and that profiles with lesser flux intensity were less likely to be constant flux. We defined strong flux as $1\times10^{13}\,m^{-2}\,s^{-1}$ or more, based on inspecting the data set for typical constant-flux profiles and on statistical work by *Ogawa et al.* [2009a].

We found that upflowing plasma showed velocity profiles that were good fits to linear functions, and we have derived equations of motion from that empirical observation in Appendix A. We calculated plasma travel times in three ways: (1) based on an empirical observation that ion velocity profiles during upflows were often well described by a straight-line fit, which implied exponential acceleration, (2) numerical integration of a fitted ion velocity profile derived from the physics of conservation of ion flux, and (3) numerical integration of the fitted velocity profiles allowing use of flux tube velocity only while overhead in the field of view of the radar giving a time variation of $v_i(z)$. The ranges of travel times calculated by the three methods were found to be in good agreement, although Method 3 suffered from poor statistics. We identify the V-shaped upflow structures seen in Figure 1b as linked to quasi-static inverted-V structures convecting across the radar beam. In two of our travel time computations, we assumed that the shape of the velocity profile, convecting with the plasma, is approximately constant. It is likely that the lifetime of the upflow event is similar to the lifetime of the accompanying PMAF. The result is a range of possible travel times between two given altitudes. The typical PMAF lifetime is 5–10 min, and that limits how far the plasma can travel in altitude before the upflow stops. The plasma must reach altitudes where wave activity is present to be accelerated into outflows. We have mostly used nominal altitude of 800 and 1000 km in our discussion, but wave activity can in some cases reach significantly further down into the ionosphere. We found that plasma from below 500 km was unlikely to be uplifted to 800 km, while plasma from 600 km was very likely to be uplifted. Other altitude ranges are shown in Table 1. In this data set, the primary controlling factor of flux was the ion upflow velocity and indirectly the plasma temperature. Variations in electron density had little influence on flux intensity relative to the bulk velocity. Ion

and electron temperatures independently were weaker predictors for flux intensity than the combined plasma temperature T_p. While all temperature-flux relationships had significant scatter, the trend is clear enough that one can define thresholds for the flux based on the temperatures, or vice versa. For example, no strong flux profiles have $T_e < 2700$ K and all strong flux profiles have $T_p > 2500$ K. Nearly all profiles with $T_p > 2800$ K are strong flux profiles. These results encourage larger statistical studies examining flux drivers in the cusp.

Appendix A: Derivation of Acceleration From Velocity Profiles

We observe that in strong upflow the ion velocity profile frequently increases approximately linearly with altitude (see, for example, Figure 4b). From this, we can model the velocity and acceleration of an upflowing volume of plasma as it rises in the ionosphere. To avoid confusion with the time-independent velocity profile v_i (or $v(z)$), we here use the name $w(t)$ for the time-dependent velocity of an upflowing parcel of plasma.

We can picture the upflowing parcel of plasma as a dot that traces the ion velocity profile as it moves upward. Since the velocity profiles are linear in (v, z) space, we can describe the velocity profile as a line parametrically

$$z(t) = Cw(t) + D \tag{A1}$$

where C and D are constants. By definition, we have

$$w(t) = \dot{z}(t) \tag{A2}$$

We can combine equations (A1) and (A2) to get a differential equation

$$z(t) = C\,\dot{z}(t) + D \tag{A3}$$

The solutions are

$$w(t) = v_0 e^{kt} \tag{A4}$$

$$z(t) = \left(z_0 - \frac{v_0}{k}\right) + \frac{v_0}{k} e^{kt} \tag{A5}$$

$$a(t) = kv_o e^{kt} = kw(t) \tag{A6}$$

where

$$k = \frac{v_1 - v_0}{z_1 - z_0} = \frac{\partial v}{\partial z} \tag{A7}$$

The instantaneous acceleration at altitude z is

$$a(z) = kv(z) \tag{A8}$$

which also applies if the assumption that the shape of the ion velocity profile is approximately constant in time does not hold. The points (v_0, z_0) and (v_1, z_1) are two chosen points that lie on the straight line in the velocity profile. In our discussion of travel times earlier in this paper, we chose these points to be the upper and lower boundaries of the motion of upflowing plasma parcels. The travel time from z_0 to z_1 is given by

$$t_1 = \frac{1}{k} \ln \frac{v_1}{v_0} \tag{A9}$$

It is then sufficient to know $v(z)$ at two altitudes simultaneously to estimate the travel time, as long as one can reasonably assume that the ion velocity profile $v(z)$ increases linearly with altitude and is constant in time for the duration of the plasma motion.

In the above we assumed a vertical direction of motion for simplicity. For field-aligned motion the longer travel direction to reach a certain altitude must be taken into account. For the ESR this effect is small.

A patch study by *Kitanoya et al*. [2011] assumed an acceleration model where upflowing plasma underwent constant acceleration so that $v(z)$ increased linearly with time, to calculate the travel time of a plasma patch from 400 to 850 km altitude, and found a travel time of 19 min. The method we described above gives 24 min travel time. Applying both methods to our data, we find that the constant acceleration model yields 20–30% shorter travel times than the exponential model when initial and final velocities and altitudes are the same. The exact percentage depends on the chosen boundary conditions. *Kitanoya et al*. [2011] had only direct measurements of the ion velocities from spacecraft and had to rely upon statistical data of ion upflow [*Ogawa et al*., 2009a] to model the starting velocity. We do not see velocity profiles consistent with constant acceleration in our data.

We do not attempt in this paper to explain the mechanism behind the acceleration, only to observe empirically that as long as the ion velocity profile can be said to be increasing linearly with altitude and be constant in time the plasma motion is well described by exponential functions.

Clearly, equations (A1)–(A4) cannot model the start of ion upflow from zero velocity, only the plasma motion once underway. Equation (A4) goes asymptotically to zero as t goes to negative infinity. Some other mechanisms must give plasma the initial "push" away from zero for equations (A4)–(A8) to apply. Such a mechanism could be too small to be detected by the coarse resolution of the ESR and still be significant at velocities <100 m/s. For this reason we have chosen to only consider upflows at velocities above 100 m/s, following the upflow definition of *Ogawa et al*. [2009a].

Acknowledgments

EISCAT is an international association supported by research organizations in Norway (NFR), Sweden (VR), Finland (SA), Japan (NIPR and STEL), China (CRIRP), the United Kingdom (STFC), Germany (DFG, till 2011), and France (CNRS, till 2005). The EISCAT data used in this publication are freely available at http://www.eiscat.se/madrigal/. This project has been sponsored by the Research Council of Norway grant number 208006/F50 and partially by NSF grant AGS-1011921. We gratefully acknowledge the Center for Space Sciences at the University of Texas at Dallas and the U.S. Air Force for providing the DMSP thermal plasma data.

M. Balikhin thanks Andrew Yau and Ian McCrea for their assistance in evaluating this paper.

References

André, M., and A. Yau (1997), Theories and observations of ion energization and outflow in the high latitude magnetosphere, *Space Sci. Rev.*, *80*(1), 27–48, doi:10.1023/A:1004921619885.

Arnoldy, R. L., K. A. Lynch, P. M. Kintner, J. Bonnell, T. E. Moore, and C. J. Pollock (1996), SCIFER—Structure of the cleft ion fountain at 1400 km altitude, *Geophys. Res. Lett.*, *23*(14), 1869–1872, doi:10.1029/96GL00475.

Barakat, A. R., and R. W. Schunk (1983), O+ ions in the polar wind, *J. Geophys. Res.*, *88*(A10), 7887–7894, doi:10.1029/JA088iA10p07887.

Bonnell, J., P. Kintner, J.-E. Wahlund, K. Lynch, and R. Arnoldy (1996), Interferometric determination of broadband ELF wave phase velocity within a region of transverse auroral ion acceleration, *Geophys. Res. Lett.*, *23*(23), 3297–3300, doi:10.1029/96GL03238.

Buchert, S. C., Y. Ogawa, R. Fujii, and A. P. van Eyken (2004), Observations of diverging field-aligned ion flow with the ESR, *Ann. Geophys.*, *22*(3), 889–899, doi:10.5194/angeo-22-889-2004.

Burchill, J. K., D. J. Knudsen, B. J. J. Bock, R. F. Pfaff, D. D. Wallis, J. H. Clemmons, S. R. Bounds, and H. Stenbaek-Nielsen (2004), Core ion interactions with BB ELF, lower hybrid, and Alfvén waves in the high-latitude topside ionosphere, *J. Geophys. Res.*, *109*, A01219, doi:10.1029/2003JA010073.

Burchill, J. K., D. J. Knudsen, J. H. Clemmons, K. Oksavik, R. F. Pfaff, C. T. Steigies, A. W. Yau, and T. K. Yeoman (2010), Thermal ion upflow in the cusp ionosphere and its dependence on soft electron energy flux, *J. Geophys. Res.*, *115*, A05206, doi:10.1029/2009JA015006.

Carlson, H. C. (2012), Sharpening our thinking about polar cap ionospheric patch morphology, research, and mitigation techniques, *Radio Sci.*, *47*, RS0L21, doi:10.1029/2011RS004946.

Carlson, H. C., T. Spain, A. Aruliah, Å. Skjæveland, and J. Moen (2012), First-principles physics of cusp/polar cap thermospheric disturbances, *Geophys. Res. Lett.*, *39*, L19103, doi:10.1029/2012GL053034.

Chaston, C. C., V. Genot, J. W. Bonnell, C. W. Carlson, J. P. McFadden, R. E. Ergun, R. J. Strangeway, E. J. Lund, and K. J. Hwang (2006), Ionospheric erosion by Alfvén waves, *J. Geophys. Res.*, *111*, A03206, doi:10.1029/2005JA011367.

Coley, W. R., R. A. Heelis, and M. R. Hairston (2003), High-latitude plasma outflow as measured by the DMSP spacecraft, *J. Geophys. Res.*, *108*(A12), 1441, doi:10.1029/2003JA009890.

Cowley, S. W. H. (1998), Excitation of flow in the Earth's magnetosphere-ionosphere system: Observations by incoherent-scatter radar, in *Polar Cap Boundary Phenomena*, edited by J. Moen, A. Egeland, and M. Lockwood, pp. 127–140, Kluwer Acad., Dordrecht, Netherlands.

Cowley, S. W. H. (2000), Magnetosphere-ionosphere interactions: A tutorial review, in *Magnetospheric Current Systems*, *Geophys. Monogr. Ser.*, vol. 118, edited by S.-I. Ohtani et al., pp. 91–106, AGU, Washington, D. C.

Dombeck, J., C. Cattell, and J. McFadden (2013), A FAST study of quasi-static structure ("Inverted-V") potential drops and their latitudinal dependence in the premidnight sector and ramifications for the current-voltage relationship, *J. Geophys. Res. Space Physics*, *118*, 5731–5741, doi:10.1002/jgra.50532.

Frederick-Frost, K. M., K. A. Lynch, P. M. Kintner, E. Klatt, D. Lorentzen, J. Moen, Y. Ogawa, and M. Widholm (2007), SERSIO: Svalbard EISCAT rocket study of ion outflows, *J. Geophys. Res.*, *112*, A08307, doi:10.1029/2006JA011942.

Hoffman, R. A., and C. S. Lin (1981), Study of inverted-V auroral precipitation events, in *Physics of Auroral Arc Formation*, *Geophys. Monogr. Ser.*, vol. 25, edited by S.-I. Akasofu and J. R. Kan, pp. 80–90, AGU, Washington, D. C.

Ivchenko, N., and G. Marklund (2001), Observation of low frequency electromagnetic activity at 1000 km altitude, *Ann. Geophys.*, *19*(6), 643–648, doi:10.5194/angeo-19-643-2001.

Jacobsen, K. S., and J. I. Moen (2010), On the correlation between Broad-Band ELF wave power and ion fluxes in the cusp, *Ann. Geophys.*, *28*(6), 1249–1261, doi:10.5194/angeo-28-1249-2010.

Karlson, K. A., M. Øieroset, J. Moen, and P. E. Sandholt (1996), A statistical study of flux transfer event signatures in the dayside aurora: The IMF By -related prenoon-postnoon asymmetry, *J. Geophys. Res.*, *101*(A1), 59–68, doi:10.1029/95JA02590.

Kintner, P. M., J. Bonnell, R. Arnoldy, K. Lynch, C. Pollock, and T. Moore (1996), SCIFER-Transverse ion acceleration and plasma waves, *Geophys. Res. Lett.*, *23*(14), 1873–1876, doi:10.1029/96GL01863.

Kintner, P. M., J. Franz, P. Schuck, and E. Klatt (2000), Interferometric coherency determination of wavelength or what are broadband ELF waves?, *J. Geophys. Res.*, *105*(A9), 21,237–21,250, doi:10.1029/1999JA000323.

Kitanoya, Y., T. Abe, A. W. Yau, T. Hori, and N. Nishitani (2011), Localized electron density enhancements in the high-altitude polar ionosphere and their relationships with storm-enhanced density (SED) plumes and polar tongues of ionization (TOI), *Ann. Geophys.*, *29*(2), 367–375, doi:10.5194/angeo-29-367-2011.

Lockwood, M., M. O. Chandler, J. L. Horwitz, J. H. Waite, T. E. Moore, and C. R. Chappell (1985), The cleft ion fountain, *J. Geophys. Res.*, *90*(A10), 9736–9748, doi:10.1029/JA090iA10p09736.

Lockwood, M., S. W. H. Cowley, P. E. Sandholt, and R. P. Lepping (1990), The ionospheric signatures of flux transfer events and solar wind dynamic pressure changes, *J. Geophys. Res.*, *95*(A10), 17,113–17,135, doi:10.1029/JA095iA10p17113.

Lockwood, M., W. F. Denig, A. D. Farmer, V. N. Davda, S. W. H. Cowley, and H. Lühr (1993), Ionospheric signatures of pulsed magnetopause reconnection at the Earth's magnetopause, *Nature*, *361*(6411), 424–428, doi:10.1038/361424a0.

Lorentzen, D. A., P. M. Kintner, J. Moen, F. Sigernes, K. Oksavik, Y. Ogawa, and J. Holmes (2007), Pulsating dayside aurora in relation to ion upflow events during a northward interplanetary magnetic field (IMF) dominated by a strongly negative IMF BY, *J. Geophys. Res.*, *112*, A03301, doi:10.1029/2006JA011757.

Lühr, H., M. Rother, W. Köhler, P. Ritter, and L. Grunwaldt (2004), Thermospheric up-welling in the cusp region: Evidence from CHAMP observations, *Geophys. Res. Lett.*, *31*, L06805, doi:10.1029/2003GL019314.

Lund, E. J., et al. (2000), Transverse ion acceleration mechanisms in the aurora at solar minimum: Occurrence distributions, *J. Atmos. Sol. Terr. Phys.*, *62*(6), 467–475, doi:10.1016/S1364-6826(00)00013-4.
Lynch, K. A., R. L. Arnoldy, P. M. Kintner, and J. Bonnell (1996), The AMICIST auroral sounding rocket: A comparison of transverse ion acceleration mechanisms, *Geophys. Res. Lett.*, *23*(23), 3293–3296, doi:10.1029/96GL02688.
Lynch, K. A., R. L. Arnoldy, P. M. Kintner, P. Schuck, J. W. Bonnell, and V. Coffey (1999), Auroral ion acceleration from lower hybrid solitary structures: A summary of sounding rocket observations, *J. Geophys. Res.*, *104*(A12), 28,515–28,534, doi:10.1029/1999JA900289.
Lynch, K. A., J. L. Semeter, M. Zettergren, P. Kintner, R. Arnoldy, E. Klatt, J. LaBelle, R. G. Michell, E. A. MacDonald, and M. Samara (2007), Auroral ion outflow: Low altitude energization, *Ann. Geophys.*, *25*(9), 1967–1977, doi:10.5194/angeo-25-1967-2007.
Moen, J., D. A. Lorentzen, and F. Sigernes (1998), Dayside moving auroral forms and bursty proton auroral events in relation to particle boundaries observed by NOAA 12, *J. Geophys. Res.*, *103*(A7), 14,855–14,863, doi:10.1029/97JA02877.
Moen, J., K. Oksavik, and H. C. Carlson (2004a), On the relationship between ion upflow events and cusp auroral transients, *Geophys. Res. Lett.*, *31*, L11808, doi:10.1029/2004GL020129.
Moen, J., M. Lockwood, K. Oksavik, H. C. Carlson, W. F. Denig, A. P. van Eyken, and I. W. McCrea (2004b), The dynamics and relationships of precipitation, temperature and convection boundaries in the dayside auroral ionosphere, *Ann. Geophys.*, *22*(6), 1973–1987, doi:10.5194/angeo-22-1973-2004.
Moen, J., X. C. Qiu, H. C. Carlson, R. Fujii, and I. W. McCrea (2008), On the diurnal variability in F2-region plasma density above the EISCAT Svalbard radar, *Ann. Geophys.*, *26*, 2427–2433.
Moen, J., H. C. Carlson, Y. Rinne, and Å. Skjæveland (2012), Multi-scale features of solar terrestrial coupling in the cusp ionosphere, *J. Atmos. Sol. Terr. Phys.*, *87–88*, 11–19, doi:10.1016/j.jastp.2011.07.002.
Ogawa, Y., R. Fujii, S. C. Buchert, S. Nozawa, S. Watanabe, and A. P. van Eyken (2000), Simultaneous EISCAT Svalbard and VHF radar observations of ion upflows at different aspect angles, *Geophys. Res. Lett.*, *27*(1), 81–84, doi:10.1029/1999GL010665.
Ogawa, Y., R. Fujii, S. C. Buchert, S. Nozawa, and S. Ohtani (2003), Simultaneous EISCAT Svalbard radar and DMSP observations of ion upflow in the dayside polar ionosphere, *J. Geophys. Res.*, *108*(A3), 1101, doi:10.1029/2002JA009590.
Ogawa, Y., S. C. Buchert, R. Fujii, S. Nozawa, and A. P. van Eyken (2009a), Characteristics of ion upflow and downflow observed with the European Incoherent Scatter Svalbard radar, *J. Geophys. Res.*, *114*, A05305, doi:10.1029/2008JA013817.
Ogawa, Y., I. Häggström, S. C. Buchert, K. Oksavik, S. Nozawa, M. Hirahara, A. P. van Eyken, T. Aso, and R. Fujii (2009b), On the source of the polar wind in the polar topside ionosphere: First results from the EISCAT Svalbard radar, *Geophys. Res. Lett.*, *36*, L24103, doi:10.1029/2009GL041501.
Ogawa, Y., S. C. Buchert, A. Sakurai, S. Nozawa, and R. Fujii (2010), Solar activity dependence of ion upflow in the polar ionosphere observed with the European Incoherent Scatter (EISCAT) Tromsø UHF radar, *J. Geophys. Res.*, *115*, A07310, doi:10.1029/2009JA014766.
Pryse, S. E., R. W. Sims, J. Moen, L. Kersley, D. Lorentzen, and W. F. Denig (2004), Evidence for solar-production as a source of polar-cap plasma, *Ann. Geophys.*, *22*, 1093–1102, doi:10.5194/angeo-22-1093-2004.
Rinne, Y., J. Moen, H. C. Carlson, and M. R. Hairston (2010), Stratification of east-west plasma flow channels observed in the ionospheric cusp in response to IMF BY polarity changes, *Geophys. Res. Lett.*, *37*, L13102, doi:10.1029/2010GL043307.
Rinne, Y., J. Moen, J. B. H. Baker, and H. C. Carlson (2011), Convection surrounding mesoscale ionospheric flow channels, *J. Geophys. Res.*, *116*, A05213, doi:10.1029/2010JA015997.
Sadler, F. B., M. Lessard, E. Lund, A. Otto, and H. Lühr (2012), Auroral precipitation/ion upwelling as a driver of neutral density enhancement in the cusp, *J. Atmos. Sol. Terr. Phys.*, *87–88*, 82–90, doi:10.1016/j.jastp.2012.03.003.
Sandholt, P. E., B. Lybekk, A. Egeland, R. Nakamura, and T. Oguti (1989), Midday auroral breakup, *J. Geomagn. Geoelectr.*, *41*(4), 371–387, doi:10.5636/jgg.41.371.
Sandholt, P. E., M. Lockwood, T. Oguti, S. W. H. Cowley, K. S. C. Freeman, B. Lybekk, A. Egeland, and D. M. Willis (1990), Midday auroral breakup events and related energy and momentum transfer from the magnetosheath, *J. Geophys. Res.*, *95*(A2), 1039–1060, doi:10.1029/JA095iA02p01039.
Sandholt, P. E., H. C. Carlson, and A. Egeland (2002), *Dayside and Polar Cap Aurora*, Kluwer Acad., Boston, Mass.
Schunk, R., and A. Nagy (2009), *Ionospheres: Physics, Plasma Physics, and Chemistry*, 2nd ed., Cambridge Univ. Press, Cambridge, U. K.
Schunk, R. W. (1988), The polar wind, in *Modeling Magnetospheric Plasma*, *Geophys. Monogr. Ser.*, vol. 44, edited by T. E. Moore et al., pp. 219–228, AGU, Washington, D. C.
Semeter, J., C. J. Heinselman, J. P. Thayer, R. A. Doe, and H. U. Frey (2003), Ion upflow enhanced by drifting F-region plasma structure along the nightside polar cap boundary, *Geophys. Res. Lett.*, *30*(22), 2139, doi:10.1029/2003GL017747.
Sharp, R. D., D. L. Carr, W. K. Peterson, and E. G. Shelley (1981), Ion streams in the magnetotail, *J. Geophys. Res.*, *86*(A6), 4639–4648, doi:10.1029/JA086iA06p04639.
Shelley, E. G., R. G. Johnson, and R. D. Sharp (1972), Satellite observations of energetic heavy ions during a geomagnetic storm, *J. Geophys. Res.*, *77*(31), 6104–6110, doi:10.1029/JA077i031p06104.
Shelley, E. G., R. D. Sharp, and R. G. Johnson (1976), Satellite observations of an ionospheric acceleration mechanism, *Geophys. Res. Lett.*, *3*(11), 654–656, doi:10.1029/GL003i011p00654.
Skjæveland, Å., J. I. Moen, and H. C. Carlson (2011), On the relationship between flux transfer events, temperature enhancements and ion upflow events in the cusp ionosphere, *J. Geophys. Res.*, *116*, A10305, doi:10.1029/2011JA016480.
Southwood, D. J. (1987), The ionospheric signature of flux transfer events, *J. Geophys. Res.*, *92*(A4), 3207–3213, doi:10.1029/JA092iA04p03207.
Strangeway, R. J., R. E. Ergun, Y.-J. Su, C. W. Carlson, and R. C. Elphic (2005), Factors controlling ionospheric outflows as observed at intermediate altitudes, *J. Geophys. Res.*, *110*, A03221, doi:10.1029/2004JA010829.
Valladares, C. E., D. T. Decker, R. Sheehan, D. N. Anderson, T. Bullett, and B. W. Reinisch (1998), Formation of polar cap patches associated with north-to-south transitions of the interplanetary magnetic field, *J. Geophys. Res.*, *103*(A7), 14,657–14,670, doi:10.1029/97JA03682.
Wahlund, J.-E., H. J. Opgenoorth, I. Häggström, K. J. Winser, and G. O. L. Jones (1992), EISCAT observations of topside ionospheric ion outflows during auroral activity: Revisited, *J. Geophys. Res.*, *97*(A3), 3019–3037, doi:10.1029/91JA02438.
Watermann, J., H. Lühr, K. Schlegel, P. Stauning, J. P. Thayer, F. Christiansen, and P. T. Newell (2005), The low-altitude cusp: Multi-point observations during the February 2002 SIRCUS campaign, in *Earth Observation With CHAMP: Results From Three Years in Orbit*, edited by C. Reigber et al., pp. 375–380, Springer, Berlin, Heidelberg, New York.
Winglee, R. M. (2000), Mapping of ionospheric outflows into the magnetosphere for varying IMF conditions, *J. Atmos. Sol. Terr. Phys.*, *62*(6), 527–540, doi:10.1016/S1364-6826(00)00015-8.
Winglee, R. M., W. Lewis, and G. Lu (2005), Mapping of the heavy ion outflows as seen by IMAGE and multifluid global modeling for the 17 April 2002 storm, *J. Geophys. Res.*, *110*, A12S24, doi:10.1029/2004JA010909.
Yau, A. W., and M. André (1997), Sources of ion outflow in the high latitude ionosphere, *Space Sci. Rev.*, *80*(1), 1–25, doi:10.1023/A:1004947203046.
Yau, A. W., T. Abe, and W. K. Peterson (2007), The polar wind: Recent observations, *J. Atmos. Sol. Terr. Phys.*, *69*(16), 1936–1983, doi:10.1016/j.jastp.2007.08.010.